

X-ray study of HLX1: intermediate-mass black hole or foreground neutron star?

Roberto Soria,^{1*} Luca Zampieri,² Silvia Zane¹ and Kinwah Wu¹

¹*Mullard Space Science Laboratory, University College London, Holmbury St Mary, Surrey RH5 6NT*

²*INAF, Osservatorio Astronomico di Padova, Vicolo dell'Osservatorio 5, I-35122, Padova, Italy*

Accepted 2010 August 19. Received 2010 August 19; in original form 2010 June 14

ABSTRACT

We re-assess the *XMM–Newton* and *Swift* observations of HLX1 to examine the evidence for its identification as an intermediate-mass black hole. We show that the X-ray spectral and timing properties are equally consistent with an intermediate-mass black hole in a high state or with a foreground neutron star with a luminosity \sim a few $\times 10^{32}$ erg s⁻¹ $\sim 10^{-6}L_{\text{Edd}}$, located at a distance of ≈ 1.5 –3 kpc. Contrary to previously published results, we find that the X-ray spectral change between the two *XMM–Newton* observations of 2004 and 2008 (going from power-law dominated to thermal dominated) is not associated with a change in the X-ray luminosity. The thermal component becomes more dominant (and hotter) during the 2009 outburst seen by *Swift* but in a way that is consistent with either scenario.

Key words: accretion, accretion discs – black hole physics – stars: neutron – X-rays: binaries – X-rays: individual: HLX1.

1 INTRODUCTION

Several theoretical arguments have been suggested for the formation of black holes (BHs) with masses $\sim 10^3$ – $10^4 M_{\odot}$, straddling the gap between stellar and nuclear supermassive BHs. However, solid observational evidence of their existence remains lacking or disputed. The bright, point-like X-ray source 2XMM J011028.1–460421 (hereafter HLX1 for simplicity), discovered by Farrell et al. (2009), has been proposed as the first unambiguous identification of an intermediate-mass BH (see also Godet et al. 2009; Webb et al. 2010). The (variable) X-ray emission from this source clearly indicates an accreting compact object rather than a star. It appears located inside or projected in front of the bulge/halo of the S0 galaxy (Farrell et al. 2009), located at a distance of ≈ 91 Mpc (Afonso et al. 2005). If HLX1 does belong to that galaxy, it reached X-ray luminosities $\approx 10^{42}$ erg s⁻¹, implying a BH mass $> 1000 M_{\odot}$ from Eddington-limit arguments (Farrell et al. 2009). Its optical counterpart (Soria et al. 2010) is a point-like source with $R \approx 24$ mag, which implies an X-ray/optical flux ratio ~ 500 – 1000 . This is consistent with an X-ray binary but rules out a background AGN, for which we would expect flux ratios ~ 0.1 – 10 . The brightness and colour of the optical counterpart are consistent with either a massive globular cluster in ESO243–49 (which may contain an accreting intermediate-mass BH) or a foreground M star in the Galactic halo (Soria et al. 2010). A residual emission line consistent with H α redshifted by the systemic velocity of ESO243–49 (Wiersema et al. 2010) seems to

provide decisive support for the intermediate-mass BH interpretation. However, the issue is still hotly debated.

In this paper, we discuss the constraints to the nature of HLX1 provided by the *XMM–Newton* and *Swift* observations, and re-examine its X-ray luminosity and spectral properties. In particular, we want to determine whether X-ray flux and spectral information are already sufficient to rule out the possibility of a foreground neutron star (NS), weakly accreting from a low-mass donor star. If that is the case, the X-ray properties of HLX1 could be used in the future as a template to identify other intermediate-mass BHs.

2 X-RAY OBSERVATIONS

XMM–Newton's European Photon Imaging Camera (EPIC) observed HLX1 on 2004 November 23 (ObsID 0204540201: serendipitously and ≈ 10 arcmin off-axis) and on 2008 November 28 (ObsID 0560180901: target observation, on-axis); see Table 1 for a summary of instrument modes and live times. Hereafter we will refer to those observations as XMM1 and XMM2. We downloaded the Observation Data Files from the public archive and used the Science Analysis System (SAS) version 9.0.0 (XMMASAS_20090615) to process and filter the event files and extract spectra. We checked that there were no background flares in either observation. For XMM1 MOS, we extracted the source spectra from a circular region of radius 45 arcsec; for XMM1 pn, we used a 25×30 arcsec² ellipse, to reduce overlapping with a chip gap and the row of pixels next to it. For XMM2 MOS and pn, we used a circular region of radius 30 arcsec, because the source is on-axis and has a narrower point spread function. We defined suitable background regions to avoid

*E-mail: roberto.soria@mssl.ucl.ac.uk

Table 1. *XMM-Newton* observation log.

Date	Instrument	Mode	Live time (ks)
2004 November 23	pn	Prime full (thin1)	18.0
	MOS	Prime full (thin1)	21.6
2008 November 28	pn	Prime small (thin1)	35.3
	MOS	Prime full (thin1)	49.9

chip gaps. We selected single and double events (pattern ≤ 4 for the pn and pattern ≤ 12 for the MOS). After building response and ancillary response files with the *SAS* tasks *rmfgen* and *arngen*, we used *XSPEC* (Arnaud 1996) version 12 for spectral fitting.

We used the *XMM2* data for timing analysis (*XMM1* being too short and affected by the chip gap problem). The science modes used for *XMM2* give a time resolution of 5.7 ms for the pn and 2.6 s for the MOS detectors. We used *XMMSELECT* to extract pn and MOS source and background light curves, selecting single and double events in the 0.2–12 keV range. We defined the same start and stop time for the pn and MOS light curves, so that they could be combined into a total EPIC light curve. This is possible because pn and MOS have a similar exposure times ≈ 50 ks, although the pn live time is only 71 per cent of the exposure time (small window mode). Background subtraction, together with corrections for various sorts of detector inefficiencies (vignetting, bad pixels, dead time, etc.), was performed with the *SAS* task *epiclccorr*. We then used standard *FTOOLS* tasks for timing analysis.

In addition, HLX1 has been the target of over 40 *Swift* X-ray Telescope (XRT) observations since 2008 October; see NASA’s HEASARC data archive for a detailed logbook. We used the online XRT data product generator (Evans et al. 2007, 2009) to extract light curves and spectra (including background and ancillary response files); we selected grade 0–12 events. We downloaded the suitable spectral response file for single and double events in photon-counting mode from the latest Calibration Data base (2009 December 1); it is the same response used by Godet et al. (2009). We grouped the *Swift* spectra into four bands, according to count rates (Section 3.3), and fitted the co-added spectra of each band with *XSPEC* version 12.

3 X-RAY SPECTRAL MODELLING

3.1 Choice of models

We chose four spectral models based on the combination of a power law with a soft thermal component, suitable to the high-accretion-state BH and/or the low-accretion-state NS scenarios. The first model is power law plus single-temperature blackbody, which gives the simplest phenomenological estimate of the soft component. The second model is power law plus disc-blackbody, suitable to the BH scenario; the thermal disc component has a much broader spectral shape than the single-temperature blackbody. The models for thermal component in the third and fourth models are suitable to fit the emission from a weakly magnetized NS hydrogen atmosphere in hydrostatic and local thermodynamical equilibrium: they are broader and harder than a simple blackbody at the same effective temperature, but slightly narrower than a standard disc-blackbody.

Blackbody (bb in *XSPEC*), disc-blackbody (diskbb; Makishima et al. 1986) and NS atmosphere (*nsa*; Zavlin, Pavlov & Shibanova 1996) models are well known from the standard release of *XSPEC* and do not require additional explanations here. Our fourth model is the *zamp* model, which has been implemented in *XSPEC* as an ad-

ditive table (Campana, Mereghetti & Sidoli 1997) using the spectra computed in Zampieri et al. (1995). The difference is that, while the *nsa* model computes the X-ray spectrum of a passively cooling NS, the *zamp* model was developed specifically to reproduce the emission from non-magnetized NSs accreting at very low rates ($10^{-7} \lesssim L/L_{\text{Edd}} \lesssim 10^{-3}$), for example from the interstellar medium, a molecular cloud, or a very low mass stellar donor (the last case may be applicable to HLX1). In fact, the X-ray spectra from *nsa* and *zamp* turn out to be virtually indistinguishable at the signal-to-noise ratio level of our data. The main reason for the similarity is that, at such low luminosities, the NS atmosphere develops smooth temperature and density gradients in the inner layers where free–free emission absorption dominates; those gradients are very similar in the two cases. The free–free opacity is a function of frequency: as a result, the emerging higher frequency photons are emitted in deeper (hotter) layers; the observed spectrum is a superposition of Planckians at different temperatures, with a broader plateau around the peak than a simple blackbody. In addition, the *zamp* model predicts a temperature inversion in the most external layers, due to accretion, but since this region is already optically thin to X-ray photons, it does not appreciably contribute to the observed X-ray spectrum. The additional power-law component is observed in weakly accreting neutron stars at luminosities $\sim 10^{32}$ erg s $^{-1}$, although its origin is still unclear (Jonker et al. 2004), perhaps associated with faint, residual magnetospheric activity. In the high-state BH scenario, the power-law component comes from a hot Comptonizing medium that reprocesses part of the thermal disc photons.

For consistency, we have used the same NS mass $M = 1.4 M_{\odot}$ and true NS radius $R = 12.4$ km for both the *zamp* and *nsa* models. The fitting parameter for the *nsa* model is the local (non-redshifted) effective temperature T_{eff} ; the effective temperature inferred by a distant observer is $T_{\text{eff}}(1 - 2GM/R)^{0.5}$. The fitting parameter for the *zamp* model is the total isotropic luminosity at infinity scaled to the Eddington luminosity, L/L_{Edd} . This can be easily related to the effective temperature, because $L = 4\pi R^2 \sigma T_{\text{eff}}^4 (1 - 2GM/R)$, assuming that the NS is isotropically emitting from the whole surface (a scaling area factor can easily be introduced when this is not the case). The fitting parameter for the bb model is the colour temperature T_{bb} seen by the distant observer (i.e. redshifted). Thus, when comparing the best-fitting temperature from those three models, we need to remember that $T_{\text{bb}} = \gamma(1 - 2GM/R)^{0.5} T_{\text{eff}} \approx 0.82\gamma T_{\text{eff}}$, where γ is the hardening factor.

3.2 XMM-Newton results

For both *XMM1* and *XMM2*, we fitted pn and MOS spectra simultaneously, leaving a free normalization constant between the three instruments. A priori, there might have been significant discrepancies due to the pn chip gap cutting across the source (in *XMM1*), or to the fact that pn and MOS were in different modes (in *XMM2*). In fact, the pn and MOS events processed and extracted with *SAS* version 9.0.0 turned out to be consistent both in spectral shape and in normalization (within 3 per cent), for both observations. This is not the case when pn and MOS event files are processed with earlier versions of the *SAS* (e.g. version 6.6.0 was used for the pipeline-processed files in the public archives); in particular, for those older versions there is an ≈ 10 per cent discrepancy between pn and MOS below 0.5 keV, which makes it difficult to get strong constraints on the soft thermal component. This may be the reason why Farrell et al. (2009, their fig. 2) chose to ignore all pn data below 0.5 keV in *XMM2*, and MOS2 data below 0.4 keV in *XMM1*, without providing any explanations.

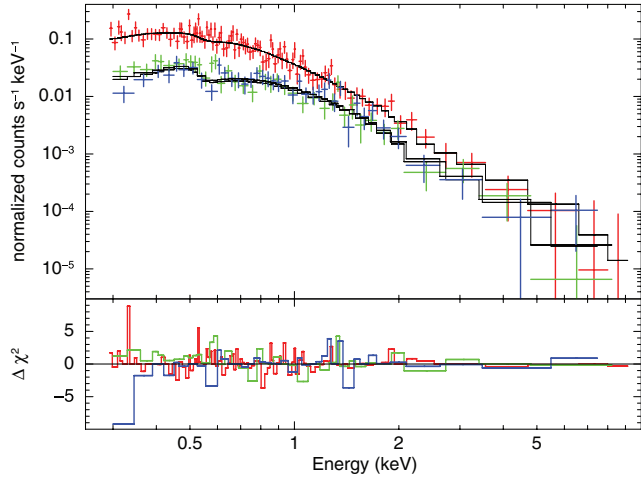


Figure 1. *XMM-Newton*/EPIC spectra from the 2004 observation, simultaneously fitted with the NS atmosphere model zamp plus power law. EPIC-pn data points and χ^2 contributions are plotted in red, MOS1 data in green and MOS2 data in blue (see Table 2 for the best-fitting parameters).

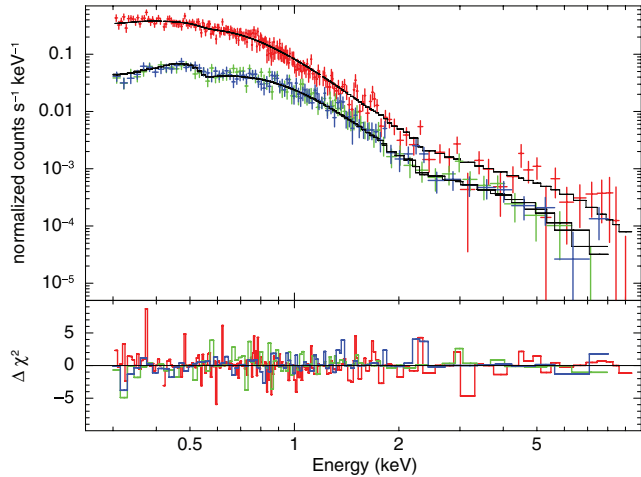


Figure 2. As in Fig. 1, for the 2008 *XMM-Newton*/EPIC spectra (see Table 3 for the best-fitting parameters).

The first result of our analysis is that the XMM1 spectrum (Fig. 1) is dominated by a power-law component, while the XMM2 spectrum (Fig. 2) is dominated by the thermal component: this is in general agreement with the results of Farrell et al. (2009) and Godet et al. (2009), and confirms their finding that there was a significant spectral transition between XMM1 and XMM2. However, unlike Farrell et al. (2009), we find that the XMM1 spectral fit is improved by the addition of a soft thermal component (F -test significance ≈ 95 per cent for each of the four thermal models used in this work). In XMM1, the thermal component carries approximately one-third of the emitted luminosity in the 0.3–10 keV band; in XMM2, it accounts for almost 80 per cent of the emitted X-ray luminosity. It is possible to introduce additional parameters, for example using low-metallicity or ionized absorbers, to obtain statistically equivalent fits without a soft thermal component for XMM1. However, the price to pay is that a steeper power-law slope is required (photon index $\Gamma > 3$, unusual for an accreting compact object). Besides, a combination of thermal and power-law components is seen in all other observations of this source (XMM2 and *Swift*); so, there are

no compelling reasons for forcing the first spectrum to be fitted by a simple power law.

When both XMM1 and XMM2 are fitted with a thermal plus power-law model, we find (Tables 2 and 3) that the unabsorbed flux is the same for both observations, $f_{0.3-10}^{\text{un}} \approx 4 \times 10^{-13} \text{ erg cm}^{-2} \text{ s}^{-1}$ (corresponding to a luminosity $\approx 4 \times 10^{41} \text{ erg s}^{-1}$ at a distance of 91 Mpc), in contrast with the findings of Farrell et al. (2009). This is important because it means that the spectral transition between XMM1 and XMM2 was more likely due to a change in the relative fraction of thermal/non-thermal photon output at constant luminosity rather than to a change in the accretion rate. There are subsequent *Swift* observations when the unabsorbed flux does increase, reaching $\approx 8 \times 10^{-13} \text{ erg cm}^{-2} \text{ s}^{-1}$ (Table 4), but their spectral properties look very different from those seen in XMM1 (Section 3.3).

The colour temperature of the thermal component is $\approx 0.13 \text{ keV}$ for both XMM1 and XMM2, when fitted with a simple blackbody model, while the effective temperature from the zamp and nsa models is $\approx 0.06 \text{ keV}$. This is expected because of the hardening effect on the photon spectrum emerging from the NS atmosphere. It implies a hardening factor of ≈ 2.7 , which is similar to what was calculated by Zampieri et al. (1995, their table 1) for this range of luminosities ($L \approx 10^{-6} L_{\text{Edd}} \approx 2 \times 10^{32} \text{ erg s}^{-1}$, in the NS scenario).

The best-fitting intrinsic column density is higher in XMM1 ($\approx 4 \times 10^{20} \text{ cm}^{-2}$) than in XMM2 ($< 10^{20} \text{ cm}^{-2}$), which is at least qualitatively consistent with the results of Farrell et al. (2009). We suggest that this may not reflect a true physical change in the source. Our X-ray spectral models of XMM1 are dominated by the phenomenological power-law component, which requires intrinsic absorption to avoid divergence at soft energies. We have tried replacing the power-law model with more complex Comptonization models, where the power-law-like component has an intrinsic turnover at low energies, around the temperature of the seed photons. We obtain equally acceptable fits (e.g. $\chi^2_{\nu} = 172.0/175$ for a comptt model) with similar seed-photon temperatures $\approx 0.1 \text{ keV}$ and no intrinsic absorption. On the other hand, XMM2 and the *Swift* spectra (Section 3.3) are dominated by the thermal component at low energies and do not require artificial addition of intrinsic absorption.

The next step is to determine whether the thermal emission is better fitted by a single-temperature or multitemperature component. We find that all four models give equivalent fits for XMM1 and XMM2. Taking into account all five sets of spectral fits (both *XMM-Newton* observations, and the three grouped data sets from *Swift*), there is a hint that a single-temperature blackbody may give a slightly worse fit than broader thermal components (Tables 2–6) but longer observations will be necessary to test this suggestion. In any case, there is no statistical difference between disc-blackbody models (most suitable to an intermediate-mass BH scenario) and NS atmosphere models. X-ray spectroscopy alone cannot rule out either scenario.

3.3 *Swift* results

Individual *Swift*/XRT observations do not have enough counts to allow two-component spectral fits and to provide any constraints on the relative contribution and temperature of the thermal component. To get around this problem, we examined the *Swift*/XRT light curve and grouped the observations into four bands, at very high (‘A’), high (‘B’), intermediate (‘C’) and low (‘D’) count rates (Fig. 3). We then co-added the spectra from all the observations in each band. Band D is still too faint for two-component spectral fitting, and we will not discuss it here. For bands A, B and

Table 2. Best-fitting spectral parameters for the 2004 *XMM-Newton*/EPIC observation. In addition to the intrinsic column density listed here, we included a line-of-sight column density of $2 \times 10^{20} \text{ cm}^{-2}$. Errors are 90 per cent confidence level for one interesting parameter. The fitting parameter for the zamp model is (L/L_{Edd}) , but we have also listed the corresponding value of kT_{eff} for an easier comparison with the other models.

Parameter	First XMM observation			
	wabs*(bb+po)	wabs*(diskbb+po)	wabs*(zamp+po)	wabs*(nsa+po)
$N_{\text{H,int}}$	$4.1^{+2.8}_{-2.9} \times 10^{20} \text{ cm}^{-2}$	$4.3^{+3.6}_{-3.4} \times 10^{20} \text{ cm}^{-2}$	$3.6^{+3.5}_{-2.9} \times 10^{20} \text{ cm}^{-2}$	$3.1^{+5.0}_{-2.9} \times 10^{20} \text{ cm}^{-2}$
kT_{bb}	$0.131^{+0.028}_{-0.027} \text{ keV}$			
N_{bb}	$1.5^{+1.1}_{-0.9} \times 10^{-6}$			
kT_{dbb}		$0.17^{+0.05}_{-0.04} \text{ keV}$		
N_{dbb}		$12.9^{+46.8}_{-10.1}$		
$\log(L/L_{\text{Edd}})$			$-6.04^{+0.49}_{-0.45}$	
N_{zam}			$2.0^{+1.3}_{-1.2} \times 10^{-5}$	
kT_{eff}			$[0.059^{+0.020}_{-0.013} \text{ keV}]$	$0.059^{+0.014}_{-0.007} \text{ keV}$
N_{nsa}				$1.8^{+32.3}_{-1.4} \times 10^{-7}$
Γ	$2.99^{+0.35}_{-0.35}$	$2.94^{+0.38}_{-0.43}$	$2.87^{+0.43}_{-0.40}$	$2.81^{+0.51}_{-0.28}$
N_{po}	$6.4^{+2.0}_{-1.8} \times 10^{-5}$	$6.1^{+2.3}_{-2.2} \times 10^{-5}$	$5.4^{+2.4}_{-2.0} \times 10^{-5}$	$5.0^{+3.2}_{-1.9} \times 10^{-5}$
$f_{0.3-10}$	$2.7^{+0.3}_{-0.3} \times 10^{-13}$	$2.7^{+0.3}_{-0.6} \times 10^{-13}$	$2.7^{+0.4}_{-0.2} \times 10^{-13}$	$2.7^{+0.3}_{-1.3} \times 10^{-13}$
$f_{0.3-10}^{\text{un}}$	$4.3^{+1.0}_{-0.7} \times 10^{-13}$	$4.4^{+1.1}_{-0.8} \times 10^{-13}$	$4.1^{+1.0}_{-0.6} \times 10^{-13}$	$4.3^{+1.5}_{-0.8} \times 10^{-13}$
χ^2_{ν}	0.99 (174.1/175)	1.00 (174.7/175)	1.00 (174.8/175)	1.00 (175.3/175)

Table 3. As in Table 1, for the 2008 *XMM-Newton*/EPIC observation.

Parameter	Second XMM observation			
	wabs*(bb+po)	wabs*(diskbb+po)	wabs*(zamp+po)	wabs*(nsa+po)
$N_{\text{H,int}}$	$<0.5 \times 10^{20} \text{ cm}^{-2}$	$<1.3 \times 10^{20} \text{ cm}^{-2}$	$<0.9 \times 10^{20} \text{ cm}^{-2}$	$0.9^{+1.3}_{-0.9} \times 10^{20} \text{ cm}^{-2}$
kT_{bb}	$0.133^{+0.003}_{-0.003} \text{ keV}$			
N_{bb}	$3.33^{+0.22}_{-0.35} \times 10^{-6}$			
kT_{dbb}		$0.186^{+0.005}_{-0.004} \text{ keV}$		
N_{dbb}		$20.4^{+13.9}_{-2.0}$		
$\log(L/L_{\text{Edd}})$			$-6.02^{+0.05}_{-0.01}$	
N_{zam}			$4.67^{+0.24}_{-0.29} \times 10^{-5}$	
kT_{eff}			$[0.060^{+0.002}_{-0.001} \text{ keV}]$	$0.055^{+0.002}_{-0.002} \text{ keV}$
N_{nsa}				$5.5^{+0.4}_{-1.3} \times 10^{-7}$
Γ	$2.62^{+0.13}_{-0.18}$	$2.03^{+0.23}_{-0.22}$	$1.89^{+0.17}_{-0.22}$	$1.82^{+0.18}_{-0.16}$
N_{po}	$3.4^{+0.4}_{-0.4} \times 10^{-5}$	$1.9^{+0.5}_{-0.4} \times 10^{-5}$	$1.5^{+0.3}_{-0.3} \times 10^{-5}$	$1.4^{+0.4}_{-0.3} \times 10^{-5}$
$f_{0.3-10}$	$3.2^{+0.1}_{-0.1} \times 10^{-13}$	$3.4^{+0.1}_{-0.1} \times 10^{-13}$	$3.4^{+0.1}_{-0.1} \times 10^{-13}$	$3.4^{+0.3}_{-0.6} \times 10^{-13}$
$f_{0.3-10}^{\text{un}}$	$3.8^{+0.2}_{-0.1} \times 10^{-13}$	$4.0^{+0.2}_{-0.1} \times 10^{-13}$	$3.9^{+0.3}_{-0.1} \times 10^{-13}$	$4.2^{+0.4}_{-0.2} \times 10^{-13}$
χ^2_{ν}	0.94 (356.5/381)	0.93 (352.6/381)	0.92 (351.7/381)	0.93 (356.2/381)

C, we used the same four spectral models applied to XMM1 and XMM2 (Tables 4–6). The total exposure time of the co-added band-A spectrum is 19.0 ks; for band B, 22.3 ks, and for band C, 67.3 ks.

We found that a thermal component is required for the combined spectrum of every band. In fact, the band-A spectrum (corresponding to the outburst peak in 2009 August) is consistent with only a thermal component (Fig. 4), without a power law, although the upper limit to the power-law normalization is not very constraining. The fractional power-law contribution becomes more important for

the band-B and band-C spectra at lower luminosities, mainly because the thermal component declines. Spectral parameters and unabsorbed flux of the band-C spectrum are very similar to those of XMM2, although at lower signal-to-noise ratio.

Putting together the *Swift* and *XMM-Newton* spectral results, we find two possible trends, which will have to be tested by longer observations. First, the relative contribution of the power-law component seems to decrease at higher luminosities (Fig. 5). This can be explained in the framework of BH accretion, if the Comptonizing region (responsible for the power-law component) collapses to an

Table 4. Best-fitting spectral parameters for the co-added *Swift*/XRT observations at the peak of the 2009 August outburst. See Fig. 3 for our definition of band A. We fixed the intrinsic column density to zero (it converges to zero even when left as a free fitting parameter). In addition, we included a line-of-sight column density of $2 \times 10^{20} \text{ cm}^{-2}$. Errors are 90 per cent confidence level for one interesting parameter.

Parameter	Band-A <i>Swift</i> observations			
	wabs*(bb+po)	wabs*(diskbb+po)	wabs*(zamp+po)	wabs*(nsa+po)
	Value			
$N_{\text{H,int}}$	0 (fixed)	0 (fixed)	0 (fixed)	0 (fixed)
kT_{bb}	$0.18^{+0.03}_{-0.02}$ keV			
N_{bb}	$9.1^{+2.7}_{-2.3} \times 10^{-6}$			
kT_{dbb}		$0.283^{+0.018}_{-0.021}$ keV		
N_{dbb}		$8.9^{+2.8}_{-2.5}$		
$\log(L/L_{\text{Edd}})$			$-5.07^{+0.13}_{-0.13}$	
N_{zam}			$25.2^{+2.4}_{-2.4} \times 10^{-5}$	
kT_{eff}			[$0.104^{+0.008}_{-0.008}$ keV]	$0.094^{+0.009}_{-0.009}$ keV
N_{nsa}				$1.2^{+0.6}_{-0.4} \times 10^{-7}$
Γ	$2.2^{+1.2}_{-0.9}$	2.0 (fixed)	2.0 (fixed)	2.0 (fixed)
N_{po}	$5.9^{+4.8}_{-5.4} \times 10^{-5}$	$<4.6 \times 10^{-5}$	$<5.1 \times 10^{-5}$	$<4.4 \times 10^{-5}$
$f_{0.3-10}$	$8.6^{+2.9}_{-0.9} \times 10^{-13}$	$7.8^{+0.2}_{-0.6} \times 10^{-13}$	$7.7^{+0.6}_{-0.7} \times 10^{-13}$	$7.7^{+1.3}_{-3.2} \times 10^{-13}$
$f_{0.3-10}^{\text{un}}$	$9.7^{+2.4}_{-0.9} \times 10^{-13}$	$8.9^{+1.1}_{-0.2} \times 10^{-13}$	$8.7^{+1.3}_{-0.2} \times 10^{-13}$	$8.8^{+1.2}_{-0.2} \times 10^{-13}$
χ^2_{ν}	0.76 (14.5/19)	0.74 (15.6/21)	0.67 (14.2/21)	0.69 (14.6/21)

Table 5. As in Table 4, for the *Swift*/XRT observations during the decline from the 2009 August outburst (as defined in Fig. 3).

Parameter	Band-B <i>Swift</i> observations			
	wabs*(bb+po)	wabs*(diskbb+po)	wabs*(zamp+po)	wabs*(nsa+po)
	Value			
$N_{\text{H,int}}$	0 (fixed)	0 (fixed)	0 (fixed)	0 (fixed)
kT_{bb}	$0.14^{+0.02}_{-0.02}$ keV			
N_{bb}	$4.9^{+2.3}_{-2.4} \times 10^{-6}$			
kT_{dbb}		$0.194^{+0.027}_{-0.024}$ keV		
N_{dbb}		$26.5^{+20.2}_{-12.2}$		
$\log(L/L_{\text{Edd}})$			$-5.92^{+0.27}_{-0.17}$	
N_{zam}			$8.0^{+3.2}_{-3.7} \times 10^{-5}$	
kT_{eff}			[$0.064^{+0.10}_{-0.06}$ keV]	$0.060^{+0.009}_{-0.007}$ keV
N_{nsa}				$5.3^{+5.5}_{-2.6} \times 10^{-7}$
Γ	$2.8^{+0.5}_{-0.4}$	$2.2^{+1.0}_{-1.6}$	2.0 (fixed)	2.0 (fixed)
N_{po}	$5.4^{+2.8}_{-2.5} \times 10^{-5}$	$2.7^{+4.2}_{-2.6} \times 10^{-5}$	$2.1^{+1.0}_{-1.2} \times 10^{-5}$	$2.0^{+1.1}_{-1.1} \times 10^{-5}$
$f_{0.3-10}$	$5.0^{+1.0}_{-0.7} \times 10^{-13}$	$5.1^{+2.0}_{-0.7} \times 10^{-13}$	$5.1^{+0.8}_{-0.5} \times 10^{-13}$	$5.1^{+1.0}_{-3.0} \times 10^{-13}$
$f_{0.3-10}^{\text{un}}$	$5.9^{+0.4}_{-0.2} \times 10^{-13}$	$6.0^{+0.7}_{-0.2} \times 10^{-13}$	$6.0^{+0.3}_{-0.3} \times 10^{-13}$	$6.1^{+0.3}_{-0.4} \times 10^{-13}$
χ^2_{ν}	1.04 (21.8/21)	1.03 (21.7/21)	0.99 (21.8/22)	1.00 (22.0/22)

optically thick disc, at high-mass accretion rates. In the framework of weakly accreting NSs, our zamp and nsa spectral fits suggest an unabsorbed 0.3–10 keV luminosity varying between $\approx 2\text{--}5 \times 10^{32} \text{ erg s}^{-1}$ (Table 7). In this luminosity range, accreting NSs are known to have a power-law and a thermal X-ray component, with the relative power-law contribution decreasing as the luminosity increases (Jonker et al. 2004, their fig. 5). Thus, the X-ray spectral evolution of HLX1 also has some apparent similarities with the behaviour of weakly accreting NSs.

The second possible trend is an increase in the temperature of the thermal component at higher luminosities (Fig. 6). This is consistent with optically thick emission from a surface of approximately fixed size, which gets hotter perhaps as a result of enhanced accretion rate; it rules out the alternative possibility of a change in the soft X-ray luminosity due to an expanding photosphere. But this scenario is equally applicable to emission from the disc around a BH or from an NS surface: in both cases, we expect $L \sim T_{\text{eff}}^4$ when the size of the X-ray emitting region is fixed.

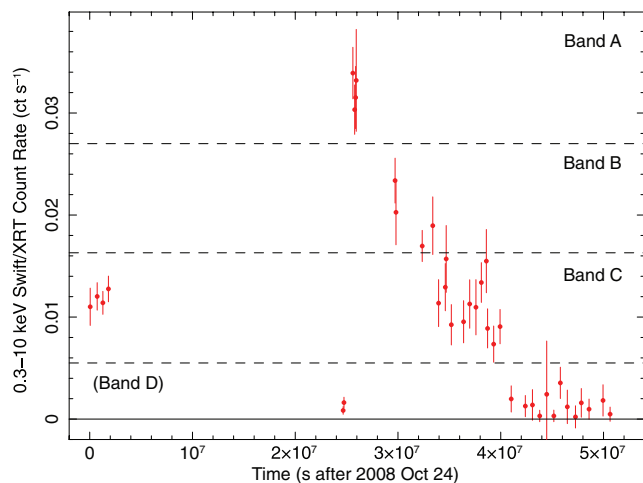
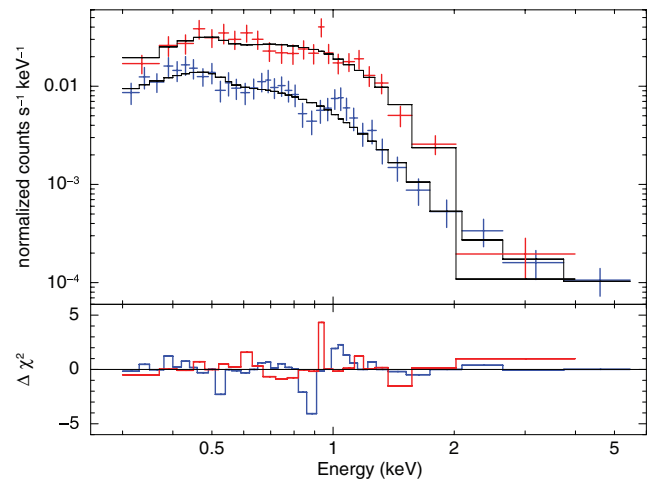
Table 6. As in Table 4, for the *Swift*/XRT observations of luminosity band C (as defined in Fig. 3).

Parameter	Band-C <i>Swift</i> observations			
	wabs*(bb+po)	wabs*(diskbb+po)	wabs*(zamp+po)	wabs*(nsa+po)
$N_{\text{H,int}}$	0 (fixed)	0 (fixed)	0 (fixed)	0 (fixed)
kT_{bb}	$0.14^{+0.02}_{-0.01}$ keV			
N_{bb}	$3.0^{+1.0}_{-1.3} \times 10^{-6}$			
kT_{dbb}		$0.204^{+0.022}_{-0.022}$ keV		
N_{dbb}		$12.5^{+7.2}_{-4.3}$		
$\log(L/L_{\text{Edd}})$			$-5.78^{+0.21}_{-0.26}$	
N_{zam}			$5.2^{+1.3}_{-1.8} \times 10^{-5}$	
kT_{eff}			[$0.069^{+0.009}_{-0.010}$ keV]	$0.066^{+0.008}_{-0.007}$ keV
N_{nsa}				$2.1^{+2.0}_{-0.8} \times 10^{-7}$
Γ	$2.2^{+1.2}_{-0.9}$	$1.5^{+0.8}_{-1.0}$	$1.4^{+0.8}_{-0.9}$	$1.2^{+1.1}_{-0.9}$
N_{po}	$3.4^{+1.8}_{-1.3} \times 10^{-5}$	$1.3^{+2.0}_{-1.0} \times 10^{-5}$	$1.1^{+1.9}_{-0.8} \times 10^{-5}$	$0.9^{+1.8}_{-0.6} \times 10^{-5}$
$f_{0.3-10}$	$3.2^{+0.3}_{-0.4} \times 10^{-13}$	$3.4^{+0.3}_{-0.9} \times 10^{-13}$	$3.4^{+0.1}_{-0.6} \times 10^{-13}$	$3.5^{+0.5}_{-2.0} \times 10^{-13}$
$f_{0.3-10}^{\text{un}}$	$3.6^{+0.2}_{-0.2} \times 10^{-13}$	$3.9^{+0.3}_{-0.2} \times 10^{-13}$	$3.9^{+0.3}_{-0.3} \times 10^{-13}$	$4.0^{+0.3}_{-0.3} \times 10^{-13}$
χ^2_{ν}	0.77 (25.6/33)	0.68 (22.5/33)	0.68 (22.6/33)	0.68 (22.4/33)

4 SHORT-TERM X-RAY VARIABILITY

The combined EPIC light curve for XMM2 does not appear particularly remarkable (Fig. 7), but it clearly suggests some short-term variability. To quantify such variability, we used the background-subtracted pn light curve binned to a time resolution of 1 s. We obtain a Kolmogorov–Smirnov probability of constancy $\approx 8 \times 10^{-3}$ and (53 ± 5) per cent rms fractional variation in excess of the Poisson level. We applied the same analysis to a combined EPIC light curve binned to 10-s intervals, obtaining a Kolmogorov–Smirnov probability of constancy 1.3×10^{-2} and (34 ± 2) per cent rms fractional variation.

We searched for characteristic periods in the pn and combined EPIC light curves, by folding the data to a range of periods (ef-search in *FTOOLS*). We do not find any strong or well-defined period; however, there is a weak, quasi-periodic modulations with


Figure 3. *Swift*/XRT light curve from 2008 October to 2010 June, with our definition of count-rate bands (see Tables 4–6 for the best-fitting parameters to the co-added spectra from bands A, B and C).

Figure 4. *Swift*/XRT spectra from band A (red) and band C (blue) fitted with the NS atmosphere model zamp plus power law. The plot highlights the significant spectral variability between the two sets of (co-added) observations. See Fig. 3 for our definition of *Swift*/XRT count-rate bands, and Tables 4–6 for the best-fitting parameters.

characteristic periods ≈ 5300 – 5600 s (Fig. 8). The power associated with this modulation or range of characteristic modulations is small, barely about the noise level, as can be seen from the power spectral density plot (Fig. 9). At higher frequencies, the power spectral density is consistent with white noise.

5 DISCUSSION AND CONCLUSIONS

We have re-examined the X-ray spectral evolution of HLX1, using two *XMM-Newton* observations from 2004 and 2008, and a series of *Swift* observations over 2008–2010. In general, a two-component model consisting of power law plus soft thermal component provides a good fit to all the spectra. The first XMM observation is

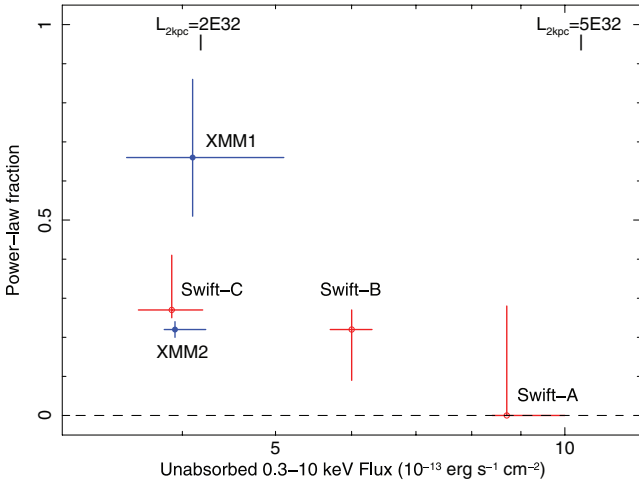


Figure 5. Fractional contribution of the power-law component to the unabsorbed 0.3–10 keV flux. The values and error bars have been calculated with the zamp model, but very similar results are obtained with the other three models. The luminosity markers are for a distance of 2 kpc (NS scenario).

Table 7. Best-fitting unabsorbed fluxes and distance to HLX1 in the NS scenario, from the normalization parameters of the zamp and nsa models (Tables 2–6).

Observation	$f_{0.3-10}^{\text{un}}$ (10^{-13} erg cm^{-2} s^{-1})	d_{zamp} (kpc)	d_{nsa} (kpc)
XMM1	$4.1^{+1.0}_{-0.6}$	$2.4^{+3.0}_{-1.3}$	$2.4^{+2.6}_{-1.9}$
XMM2	$3.9^{+0.3}_{-0.1}$	$1.8^{+0.1}_{-0.1}$	$1.3^{+0.2}_{-0.1}$
Swift-A	$8.7^{+1.3}_{-0.2}$	$3.6^{+0.6}_{-0.9}$	$2.9^{+0.6}_{-0.5}$
Swift-B	$6.0^{+0.3}_{-0.3}$	$1.6^{+0.5}_{-0.5}$	$1.4^{+0.5}_{-0.4}$
Swift-C	$3.9^{+0.3}_{-0.3}$	$2.5^{+0.8}_{-0.7}$	$2.2^{+0.6}_{-0.6}$

dominated by the power-law emission (contributing approximately two-third of the flux) but a thermal component with a colour temperature ≈ 0.13 keV is also significantly detected. Conversely, at the peak of the *Swift* outburst, the X-ray spectrum is dominated by a thermal component with a colour temperature ≈ 0.2 keV.

Although the relative contributions of thermal component and power law are significantly different between the *XMM-Newton* observations, the unabsorbed flux is similar and a factor of 2 lower than previously claimed (Farrell et al. 2009). We attribute this discrepancy to our processing of the EPIC event files with the latest version of the SAS, which may provide more accurate results at energies $\lesssim 0.5$ keV. With our re-analysis, pn and MOS now give identical spectral parameters and normalizations consistent within 3 per cent, even below 0.5 keV. As an aside, we note that the spectral difference between the two *XMM-Newton* observations was visually exaggerated in Farrell et al. (2009) by their choice of plotting two unfolded spectra based on different models (simple power law, and disc-blackbody plus power law).

For the thermal component, there is no statistical difference between disc-blackbody models (most suitable to an intermediate-mass BH scenario) and NS atmosphere models. X-ray spectroscopy alone cannot rule out either scenario. The diskbb model is normalized in terms of apparent inner-disc radius (assumed to coincide with the radius of the innermost stable circular orbit, at high accretion rates). Normalization values ~ 10 –20 (Tables 2 and 3) agree with the findings of Farrell et al. (2009) and would correspond to

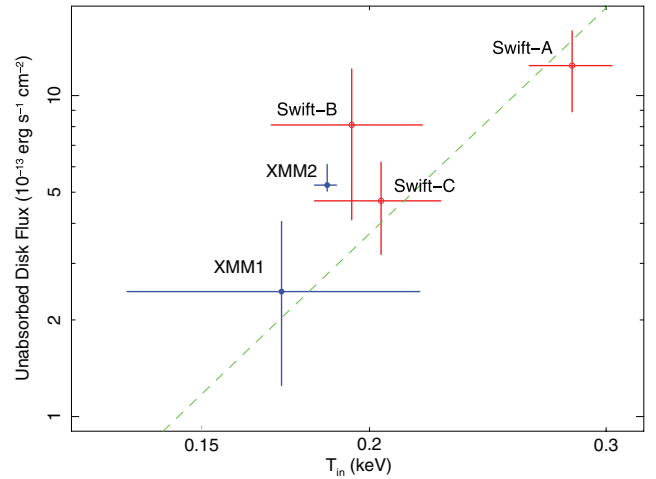


Figure 6. Relation between peak colour temperature of the best-fitting diskbb model and total unabsorbed flux in the diskbb component. The dashed line is not a fit to the data: it marks the location of the $L \propto T^4$ correlation, expected for optically thick thermal emission from a region of constant area at increasing accretion rate (inner disc or NS surface). Very similar relations between thermal luminosity and temperature are obtained with the other three spectral models.

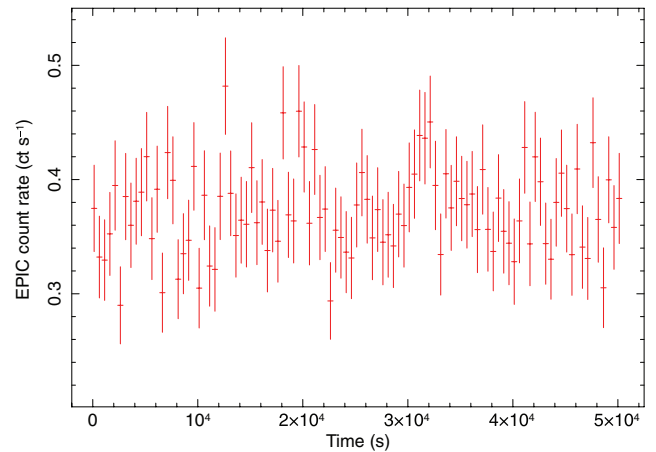


Figure 7. Combined pn + MOS light curve in the 0.2–12 keV range, binned to a time resolution of 500 s.

a BH mass $\sim 10^4 M_{\odot}$ at the distance of 91 Mpc, even higher than conservatively estimated from the Eddington limit. The small differences (less than a factor of 2) between the fitted radii over the five sets of observations may be due to the fact that the inner disc is not always extending precisely to the innermost stable circular orbit as well as to other effects such as the degree of Comptonization and spectral hardening. If HLX1 belongs to ESO243–49, our spectral fits imply emitted luminosities $\approx 4 \times 10^{41}$ erg s^{-1} in the 0.3–10 keV band, during the 2004 and 2008 *XMM-Newton* observations, rising to $\approx 10^{42}$ erg s^{-1} at the peak of the 2009 August outburst.

The zamp and nsa models are normalized in terms of distance to the source, assuming uniform emission from the surface of a $1.4 M_{\odot}$ NS with a radius of 12.4 km. Both models suggest a distance ≈ 1.5 –3 kpc (Table 7). The small discrepancies between the fitted distances over the five sets of observations may be due to the fact that the emission is never perfectly isotropic from the whole NS surface. If HLX1 is a weakly accreting NS, its 0.3–10 keV luminosity varies between $\approx (2$ –5) $\times 10^{32}$ erg s^{-1} , i.e. $\sim 10^{-6} L_{\text{Edd}}$.

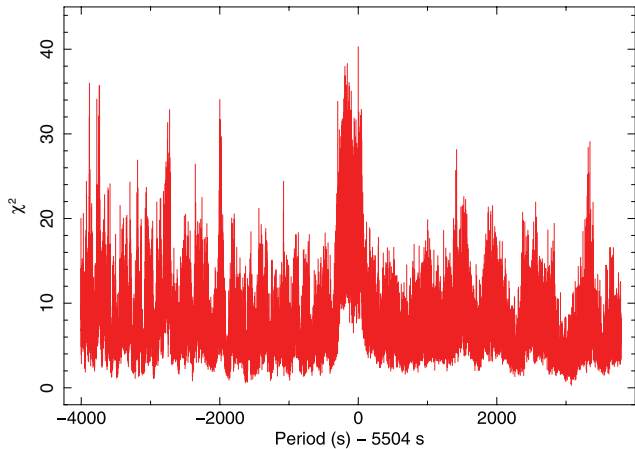


Figure 8. A search for periodicities in the combined EPIC light curve suggests the presence of weak, quasi-periodic modulations with characteristic periods $\approx 5300\text{--}5600$ s and possibly other weak features in the $1000\text{--}10\,000$ s range.

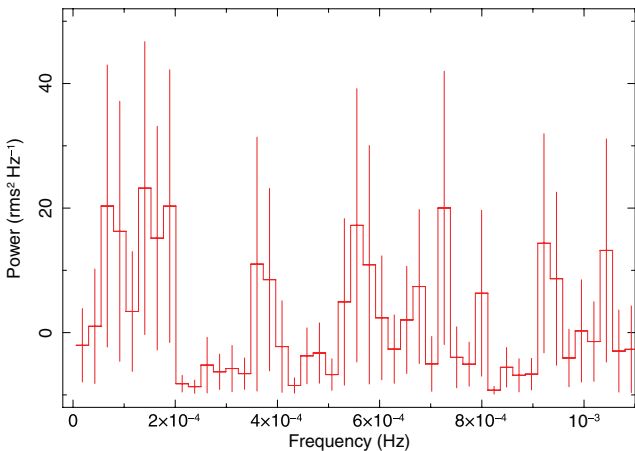


Figure 9. Low-frequency section of the power spectral density for the combined EPIC light curve. The fitted white noise level has been subtracted (normalization parameter = -2 in the `FTOOLS` task `powspec`).

This requires accretion rates $\dot{M} \sim 10^{-13} M_{\odot} \text{yr}^{-1}$. At a distance of 2 kpc, the optical counterpart found by Soria et al. (2010) would be a main-sequence M star. We also note that any direct X-ray emission from the M dwarf donor would be several orders of magnitude below our detection limit: the maximum X-ray luminosity of such stars is $\approx 10^{29} \text{ erg s}^{-1}$ (Schmitt, Fleming & Giampapa 1995; James et al. 2000).

The increase in the temperature and luminosity of the thermal component during the 2009 outburst, and the decrease of the fractional contribution of the power-law component, may be consistent both with a disc-dominated, high-state BH and with a quiescent low-mass NS X-ray binary (in particular, it is typically seen in NS X-ray binaries with X-ray luminosities $10^{32} \lesssim L_x \lesssim 10^{33} \text{ erg s}^{-1}$). In HLX1, the power-law component itself is not constant, as we can see by comparing XMM1 with XMM2 and with the very faint band-D *Swift* observations. In weakly accreting NSs, it was suggested, based on the sample of Jonker et al. (2004), that the power-law component could represent a constant baseline luminosity at $\approx 10^{32} \text{ erg s}^{-1}$ for most sources, while the thermal component increases with flux. But other quiescent NS X-ray binaries contradict this picture, because they decline to luminosities (including the power-law component)

$\lesssim 5 \times 10^{31} \text{ erg s}^{-1}$ (Heinke, Grindlay & Edmonds 2005) or even $\lesssim 3 \times 10^{30} \text{ erg s}^{-1}$ (1H 1905+000; Jonker et al. 2007). Evidence of flux variability in both the thermal and power-law components is sometimes clearly seen in quiescent NSs (Cackett et al. 2005; Jonker et al. 2005), but it is still not clear how the variability of the two components may be related because we do not know the physical origin of the faint power-law component.

The X-ray outburst and spectral variability seen in 2009 may be explained as ‘canonical’ state transitions of BH accretion. But they can also be interpreted in terms of sporadic accretion on to the surface of an NS with a low-mass donor. Material may accumulate at the magnetospheric radius, then be sporadically ‘flushed’ down towards the NS, because of the changes either in the mass transfer rate from the donor star or in the alignment of non-dipole components of the NS field.

The presence of a variable power-law component (dominant contribution in XMM1, less important in XMM2 and even less in the bright *Swift* state), with a variable photon index $\approx 2\text{--}3$, does not unambiguously identify BH or NS accretion. The power-law emission may come from inverse-Compton scattering of the soft X-ray photons by more energetic electrons in a hot corona, located either above the inner accretion disc or the NS surface. Observationally, the NS X-ray binary Aql X-1 shows X-ray spectral variability in quiescence, probably due to variable residual accretion: it has a soft thermal component with effective temperature varying between ≈ 0.11 and 0.13 keV , and a power-law component with photon index varying between ≈ 1.5 and ≈ 4 , or disappearing altogether (Rutledge et al. 2002; Campana & Stella 2003). Cen X-4 is another quiescent NS X-ray binaries well fitted by a soft thermal component ($kT \approx 0.16 \text{ keV}$) plus power law ($\Gamma \sim 2$) when its X-ray luminosity was $\sim \text{a few} \times 10^{32} \text{ erg s}^{-1}$ (Asai et al. 1996; Campana et al. 1998, 2004). Variability of the thermal component in quiescence was found by Cackett et al. (2010). Other quiescent NS X-ray binaries with comparable contributions from a soft thermal and a power-law component are listed in Jonker et al. (2004). Quiescent low-mass X-ray binary with X-ray luminosities $\sim 10^{32} \text{ erg s}^{-1}$, a thermal component and a steep ($\Gamma > 2$) power-law component were observed in the globular cluster 47 Tuc (W37 and X4; Heinke et al. 2005). Short-term X-ray variability was also seen in some observations of Aql X-1 (at 32 per cent rms; Rutledge et al. 2002) and Cen X-4 (at 45 per cent rms; Campana et al. 2004). In fact, it was suggested (Heinke et al. 2003a,b) that the strength of the power-law component and the presence of intrinsic short-term variability in quiescent NS low-mass X-ray binaries are two indicators of continued low-level accretion. The (speculative) detection of weak modulations around $\approx 5300\text{--}5600$ s can have many explanations and does not uniquely identify an intermediate-mass BH. For example, it is also the orbital period of an M4 main-sequence star filling its Roche lobe, from the well-known period–density relation in binary systems (Frank, King & Raine 2002).

In conclusion, our X-ray spectral and timing analysis has provided more accurate constraints on the unabsorbed flux, degree of variability, relative thermal/non-thermal contribution and temperature of the thermal component from HLX1. However, X-ray properties alone are not sufficient to rule out either of the competing models previously suggested for this source (old NS with a low-mass donor in the Galactic halo, or intermediate-mass BH in ESO 243–49). This is because the thermal component is equally consistent with emission from an accretion disc around a BH or from the NS surface, and the presence of an additional power-law component does not unambiguously identify the BH scenario, either. The X-ray spectral properties are consistent not only with an

intermediate-mass BH in the high or very high state but also with a quiescent NS with low-level (and variable) residual accretion. X-ray variability properties are also consistent with both scenarios. We suggest that, regardless of the true nature of HLX1, its X-ray properties do not yet provide a unique observational signature for the identification of the new class of intermediate-mass BHs. Therefore, the identification of HLX1 as an intermediate-mass BH must rely on its properties in other bands, for example from optical spectroscopy (Wiersema et al. 2010).

ACKNOWLEDGMENTS

This work made use of data supplied by the UK Swift Science Data Centre at the University of Leicester. We thank Sergio Campana for providing the `xSPEC` implementation of our models. We thank Rosanne Di Stefano, Jeanette Gladstone, Alister W. Graham, George Hau, Craig Heinke, Albert Kong, Jifeng Liu and Mat Page for useful suggestions and discussions. RS carried out part of this work while visiting Tsinghua University in Beijing.

REFERENCES

- Afonso J., Georgakakis A., Almeida C., Hopkins A. M., Cram L. E., Mobasher B., Sullivan M., 2005, *ApJ*, 624, 135
- Arnaud K. A., 1996, in Jacoby G., Barnes J., eds, *ASP Conf. Ser. Vol. 101, Astronomical Data Analysis Software and Systems V*. Astron. Soc. Pac., San Francisco, p. 17
- Asai K., Dotani T., Mitsuda K., Hoshi R., Vaughan B., Tanaka Y., 1996, *PASJ*, 48, 257
- Cackett E. M. et al., 2005, *ApJ*, 620, 922
- Cackett E. M., Brown E. F., Miller J. M., Wijnands R., 2010, *ApJ*, 720, 1325
- Campana S., Stella L., 2003, *ApJ*, 597, 474
- Campana S., Mereghetti S., Sidoli L., 1997, *A&A*, 320, 783
- Campana S., Colpi M., Mereghetti S., Stella L., Tavani M., 1998, *A&AR*, 8, 279
- Campana S., Israel G. L., Stella L., Gastaldello F., Mereghetti S., 2004, *ApJ*, 601, 474
- Evans P. A. et al., 2007, *A&A*, 469, 379
- Evans P. A. et al., 2009, *MNRAS*, 397, 1177
- Farrell S. A., Webb N. A., Barret D., Godet O., Rodrigues J. M., 2009, *Nat*, 460, 73
- Frank J., King A., Raine D. J., 2002, *Accretion Power in Astrophysics*. Cambridge Univ. Press, Cambridge
- Godet O., Barret D., Webb N. A., Farrell S. A., Gehrels N., 2009, *ApJ*, 705, L109
- Heinke C. O., Grindlay J. E., Edmonds P. D., Lloyd D. A., Murray S. S., Cohn H. N., Lugger P. M., 2003a, *ApJ*, 590, 809
- Heinke C. O., Grindlay J. E., Lugger P. M., Cohn H. N., Edmonds P. D., Lloyd D. A., Cool A. M., 2003b, *ApJ*, 598, 501
- Heinke C. O., Grindlay J. E., Edmonds P. D., 2005, *ApJ*, 622, 556
- James D. J., Jardine M. M., Jeffries R. D., Randich S., Collier Cameron A., Ferreira M., 2000, *MNRAS*, 318, 1217
- Jonker P. G., Galloway D. K., McClintock J. E., Buxton M., Garcia M., Murray S., 2004, *MNRAS*, 354, 666
- Jonker P. G., Campana S., Steeghs D., Torres M. A. P., Galloway D. K., Markwardt C. B., Chakrabarty D., Swank J., 2005, *MNRAS*, 361, 511
- Jonker P. G., Steeghs D., Chakrabarty D., Juett A. M., 2007, *ApJ*, 665, L147
- Makishima K., Maejima Y., Mitsuda K., Bradt H. V., Remillard R. A., Tuohy I. R., Hoshi R., Nakagawa M., 1986, *ApJ*, 308, 635
- Rutledge R. E., Bildsten L., Brown E. F., Pavlov G. G., Zavlin V. E., 2002, *ApJ*, 577, 346
- Schmitt J. H. M. M., Fleming T. A., Giampapa M. S., 1995, *ApJ*, 450, 392
- Soria R., Hau G. K. T., Graham A. W., Kong A. K. H., Kuin N. P. M., Li I.-H., Liu J.-F., Wu K., 2010, *MNRAS*, 405, 870
- Webb N. A., Barret D., Godet O., Servillat M., Farrell S. A., Oates S. R., 2010, *ApJ*, 712, L107
- Wiersema K., Farrell S. A., Webb N., Servillat M., Maccarone T. J., Barret D., Godet O., 2010, *ApJ*, 721, L102
- Zampieri L., Turolla R., Zane S., Treves A., 1995, *ApJ*, 439, 849
- Zavlin V. E., Pavlov G. G., Shibanov Y. A., 1996, *A&A*, 315, 141

This paper has been typeset from a $\text{\TeX}/\text{\LaTeX}$ file prepared by the author.